RSC Advances

PAPER

View Article Online
View Journal | View Issue

Cite this: *RSC Adv.*, 2026, **16**, 8255

Glutathione-responsive deformable manganese-based nanomedicines for enhanced tumor-specific chemotherapy

Pengcheng Li,†[a] Jun Tao, †*[bc] Xinzeyu Yi,†[a] Qinghui Qi,[b] Zhou Liang,[b] Ye Wu,[a] Wubulitalipu Xirena,[a] Chenxian Ye,[a] Yunqin Ke,[a] Lianhui Wang *[b] and Wanrong Yi*[a]

Improving the efficiency of drug delivery and minimizing drug-related toxicities and side effects have consistently remained key goals for tumor-specific chemotherapy. However, the intricate *in vivo* biological barriers not only impede the efficient accumulation of nanomedicines in tumors but also trigger premature drug leakage, ultimately resulting in chemotherapy failure. Herein, glutathione-responsive deformable manganese-based nanomedicines (DMNs) were constructed. Endowed with the property of glutathione-responsive stiffness transformation, the prepared DMNs could overcome *in vivo* delivery barriers, including those related to *in vivo* distribution, cellular uptake, and tissue penetration. Concomitantly, the synchronous but separate delivery of Mn^{2+} and dopamine (DA) allowed for the *in situ* triggering of Mn–DA formation, thereby enabling osteosarcoma (OS) oxidative damages. *In vitro* and *in vivo* experiments reveal that their enhanced cellular uptake, multicellular spheroid penetration, and tumor accumulation, increased by 17.64-fold, 2.25-fold and 1.6-fold, compared to that of the stiff counterpart, respectively. Additionally, an excellent specific chemotherapy efficacy with tumor growth inhibition was realized in a mice OS model, by intravenous administration of DMNs. In conclusion, glutathione-responsive deformable manganese-based nanomedicines demonstrate clinical potential by addressing the limitations of precision manganese and dopamine delivery and achieving enhanced tumor-specific chemotherapy for osteosarcoma.

Received 8th January 2026
Accepted 5th February 2026

DOI: 10.1039/d6ra00177g

rsc.li/rsc-advances

1. Introduction

Osteosarcoma, characterized by rapid progression, high malignancy and metastatic potential, and significant prognostic variability, poses a severe threat to patients' life, physical function, and quality of life.[1–3] Currently, the mainstream clinical osteosarcoma treatment approach is surgery combined with pre- and post-operative chemotherapy, while pre- and post-operative chemotherapy is prone to inducing myelosuppression (such as leukopenia increasing infection risk, thrombocytopenia causing bleeding tendency, and anemia leading to fatigue) or hepatorenal impairment.[4] These adverse effects not only reduce patients' treatment tolerance but also may force adjustments to the treatment plan due to side effects, ultimately compromising the overall therapeutic outcome.[5]

Tumor-specific chemotherapy,[6] a potential strategy in osteosarcoma treatment, relies on advanced nano-systems to precisely pre-deliver non-cytotoxic drug precursors to tumor tissues, avoiding the unintended damage to normal cells.[7] Afterwards, these non-cytotoxic drug precursors are specifically activated to highly toxic chemotherapeutic drugs within tumor cells through chemical reactions or structural transformation in response to the inherent microenvironment differences between the tumor and normal tissues (*e.g.*, overexpressed specific enzymes, acidic pH, and high glutathione concentration at the tumor site).[8,9] For example, Zhao *et al.* constructed glutathione-responsive liposomal nanoparticles (LNPs) co-loaded with Cu^{2+} and disulfiram (DSF) to enhance the efficacy of DSF-based chemotherapy. Upon exposure to intracellular glutathione, the Cu^{2+} encapsulated in LNPs' internal cavity and dithiocarbamate (DTC) generated *via* the decomposition of DSF combined *in situ* to form $Cu(DTC)_2$ complexes, which ultimately induced tumor cell death.[8] This intra-tumoral *in situ* activation strategy not only significantly reduces normal cell damage caused by premature drug leakage and lowers the incidence of side effects such as myelosuppression and hepatorenal impairment but also markedly enhances drug accumulation at the tumor site, providing a new pathway for optimizing the therapeutic efficacy of osteosarcoma treatment.[10,11]

[a]*Department of Orthopedic Trauma and Microsurgery, Zhongnan Hospital of Wuhan University, Wuhan 430071, P. R. China. E-mail: yiwanrong@whu.edu.cn*

[b]*State Key Laboratory of Flexible Electronics (LoFE), Jiangsu Key Laboratory of Smart Biomaterials and Theragnostic Technology, Institute of Advanced Materials (IAM), Nanjing University of Posts & Telecommunications, Nanjing 210023, China. E-mail: iamjtao@njupt.edu.cn; iamlhwang@njupt.edu.cn*

[c]*State Key Laboratory of Quality Research in Chinese Medicine, Institute of Chinese Medical Sciences, University of Macau, Taipa, Macau, SAR 999078, P. R. China*

† These authors contributed equally to this work.

Recently, it is reported that *in vivo* biological barriers to circulation, non-specific distribution, tissue penetration[12–14] and cellular uptake of nanomedicines limit their delivery and treatment efficiency.[15] Therefore, diverse physicochemical properties (size,[16] morphology,[17,18] electronegativity,[19] hydrophilicity, *etc.*) of nanomedicines have been broadly regulated to overcome these barriers. The mechanical property (stiffness),[20] as a curial physicochemical property of nanomedicines, has been proven to be able to manipulate nanoparticle–biology interaction. For instance, soft nanoparticles with decreased Young's modulus can penetrate deep into solid tumors through their own deformation, or improve cellular uptake by altering endocytic pathways. Nevertheless, their stiff counterparts are beneficial for non-specific distribution.[21] Fully leveraging the advantages of NPs' mechanical property holds promise for overcoming multiple biological barriers and achieving upgraded drug delivery.

Herein, a glutathione-responsive deformable manganese-based nanomedicines (DMNs) were constructed for enhanced OS-specific chemotherapy. Typically, the prepared polydopamine-coated manganese silicate nanoparticles can respond to the intracellular glutathione/pH and subsequently degrade to release Mn^{2+} and DA, accompanied by a decrease in DMNs' own stiffness. The stiffness-transformed DMNs presented significant enhancements in cellular uptake (17.64-fold), 3D multicellular spheroid penetration (2.25-fold), and tumor accumulation (1.6-fold). In addition, the formed binary coordination complex (Mn–DA) significantly promotes electron delocalization and synergistically upregulates cellular oxidative stress, resulting in OS oxidative damages.

2. Results and discussion

2.1. Synthesis and characterization of DMNs

The deformable manganese-based nanomedicines (DMNs) were synthesized *via* a mesoporous organosilica-assisted hard template method. Briefly, the pre-fabricated negatively charged mesoporous organosilica nanoparticles (MONs) were dispersed in ethylene imine polymer (PEI) solution to construct MONs-PEI though electrostatic adsorption. Subsequently, the positively charged MONs-PEI were fully oxidized by permanganate ions (MnO_4^-) into manganese silicate nanoparticles with organic–inorganic hybrid Si–R–Mn framework (MSNs). Afterwards, residual MnO_4^- on MSNs surface was reduced to MnO_2 using oil acid (OA), enabling efficient chelation of dopamine (DA) to form polydopamine (PDA) coated MSNs (DMNs). Transmission electron microscopy (TEM) images presented uniform and smooth spherical MONs with a size of 250 nm (Fig. 1a). Upon Si–R–Mn framework and surface PDA modification, high-magnification TEM and scanning electron microscopy (SEM) images revealed the crumpled spherical morphology, rough interior and folded surface of DMNs (Fig. 1b). These

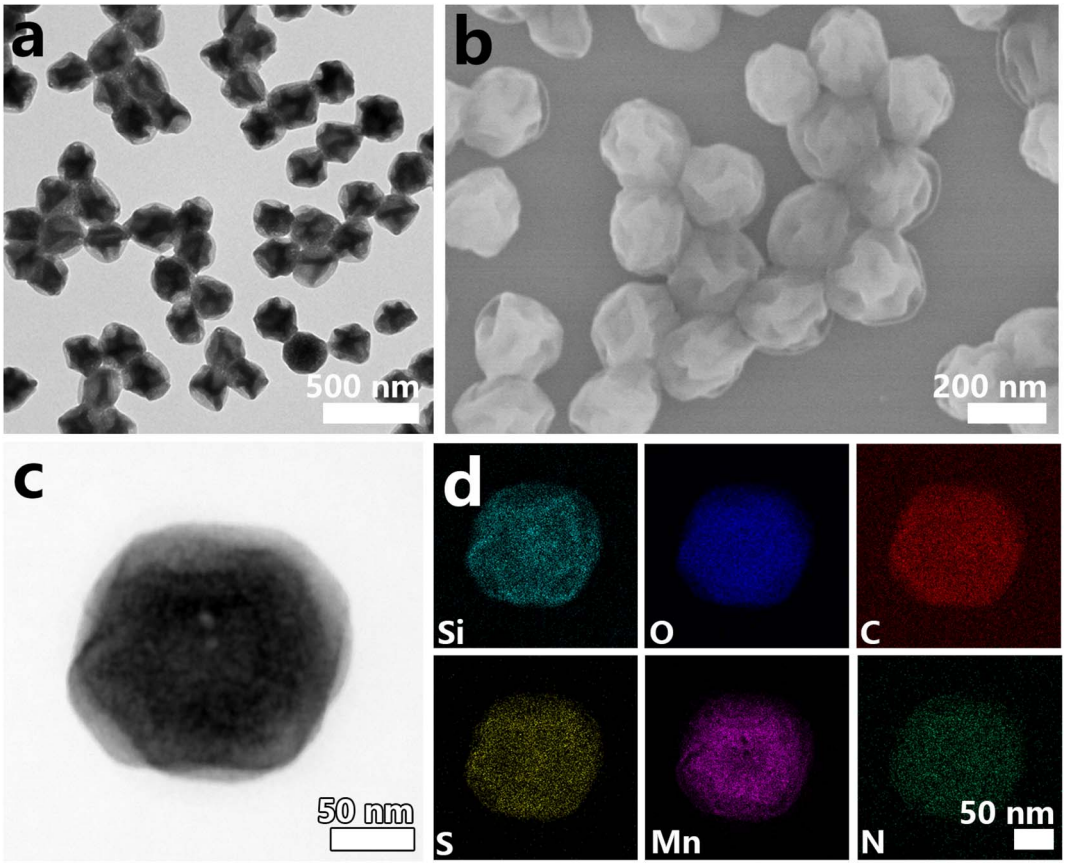

Fig. 1 TEM (a) and SEM (b), HAADF (c) and element mapping (Si, O, C, S, Mn, N) images of DMNs (d).

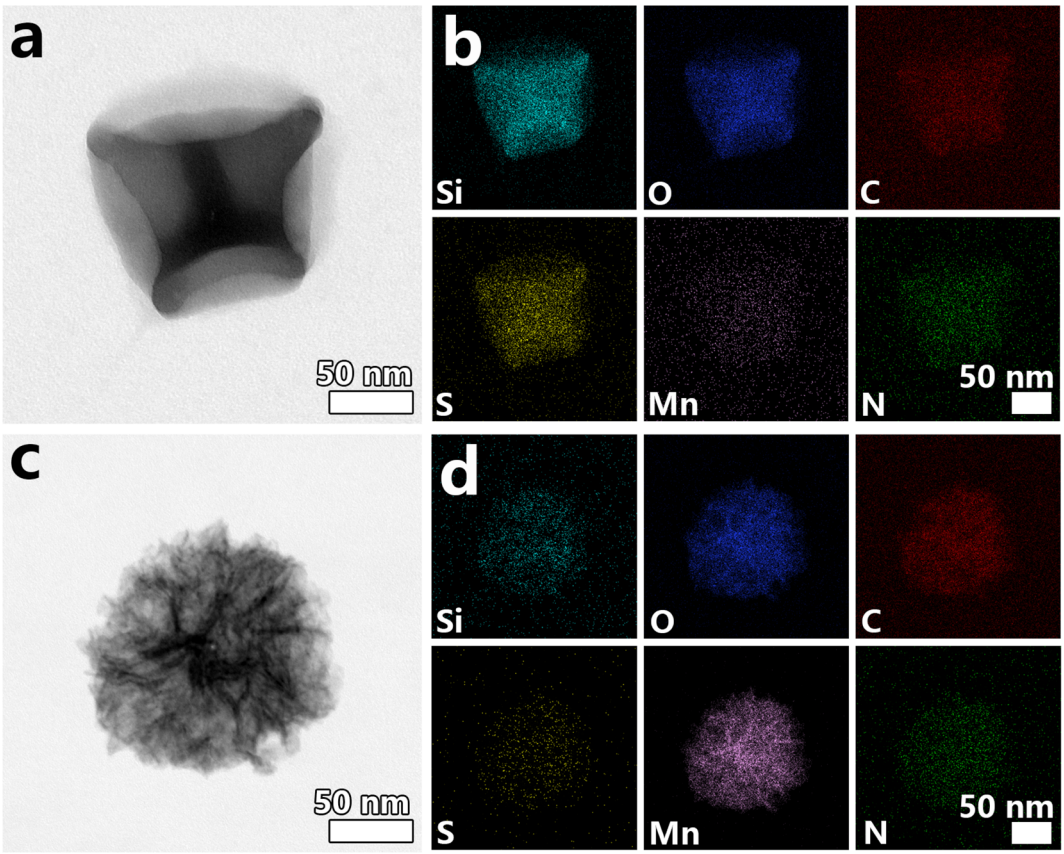

Fig. 2 TEM and element mapping (Si, O, C, S, Mn, N) images of DMNs within GSH treatment (a and b), and within NaOH treatment (c and d).

discrepancies were mainly caused by the reversal of the ratio of stiff Si–O–Si (decrease) and soft Si–R–Si (increase) inside framework. Elemental mapping images displayed the symmetrical distribution of Si and S elements and concentrated distribution of Mn element in DMNs (Fig. 1c and d), demonstrating their organic-inorganic hybrid Si–R–Mn framework. Electron dispersive spectroscopy (EDS) confirmed that mass ratio of Mn and Si inside DMNs were 48.93% and 13.96%, respectively (Fig. S1). A high proportion of Mn was highly beneficial for stiffness transformation and Mn-mediated tumor special chemotherapy. The hydrodynamic size of DMNs in PBS solution was 290 nm (Fig. S2), which was approximately consistent with the size measured in the TEM image (Fig. S3), and their morphology also remained unchanged, demonstrating their excellent stability. In addition, the zeta potential of DMNs increased to −11 mV (from −16 mV), suggesting the successful DA loading (Fig. S4).

2.2. Glutathione-responsive manganese release

To investigate their glutathione-responsive manganese release performance, these DMNs were dispersed in 10 mM of GSH solution. TEM images displayed that these crumpled stiff spherical DMNs transformed into deformable collapsed star-shaped nanocapsules with a diameter of 250 nm (Fig. 2a), concomitant with a distinct color change of the solution from brown to milky white. Corresponding element mapping images demonstrated that Si, O, and S elements maintained uniformly distributed within the framework (Fig. 2b). In contrast, the Mn element inside DMNs was nearly undetectable. These phenomena collectively indicated that the stiff Si–R–Mn structure within DMNs underwent a sensitive transition to the deformable organosilica (Si–R–Si) configuration in the GSH solution. Additionally, the degradation behavior of DMNs in alkaline solutions was also evaluated. As shown in Fig. 2c, TEM images indicated that, upon treatment with NaOH for 30 min, the wrinkled stiff spherical morphology of DMNs transformed into stiff dendritic particles, whereas the particle size and solution color remained unchanged. Element mapping images confirmed the enrichment of Mn and O elements as well as the depletion of Si and S elements (Fig. 2d), which verified the selective degradation of the organosilica moiety and the presence of residual manganese oxide within DMNs in an alkaline environment. These results perfectly confirmed that Mn element inside DMNs was crucial in initiating their own stiffness transformation.

2.3. Cellular uptake and multicellular spheroids penetration

The effects of Mn release-induced stiffness transformation of DMNs on cellular uptake and multicellular spheroids penetration were further evaluated within K7M2 cell. Firstly, the cellular internalization of DMNs was observed using biological TEM (Fig. 3a). TEM image revealed the presence of numerous

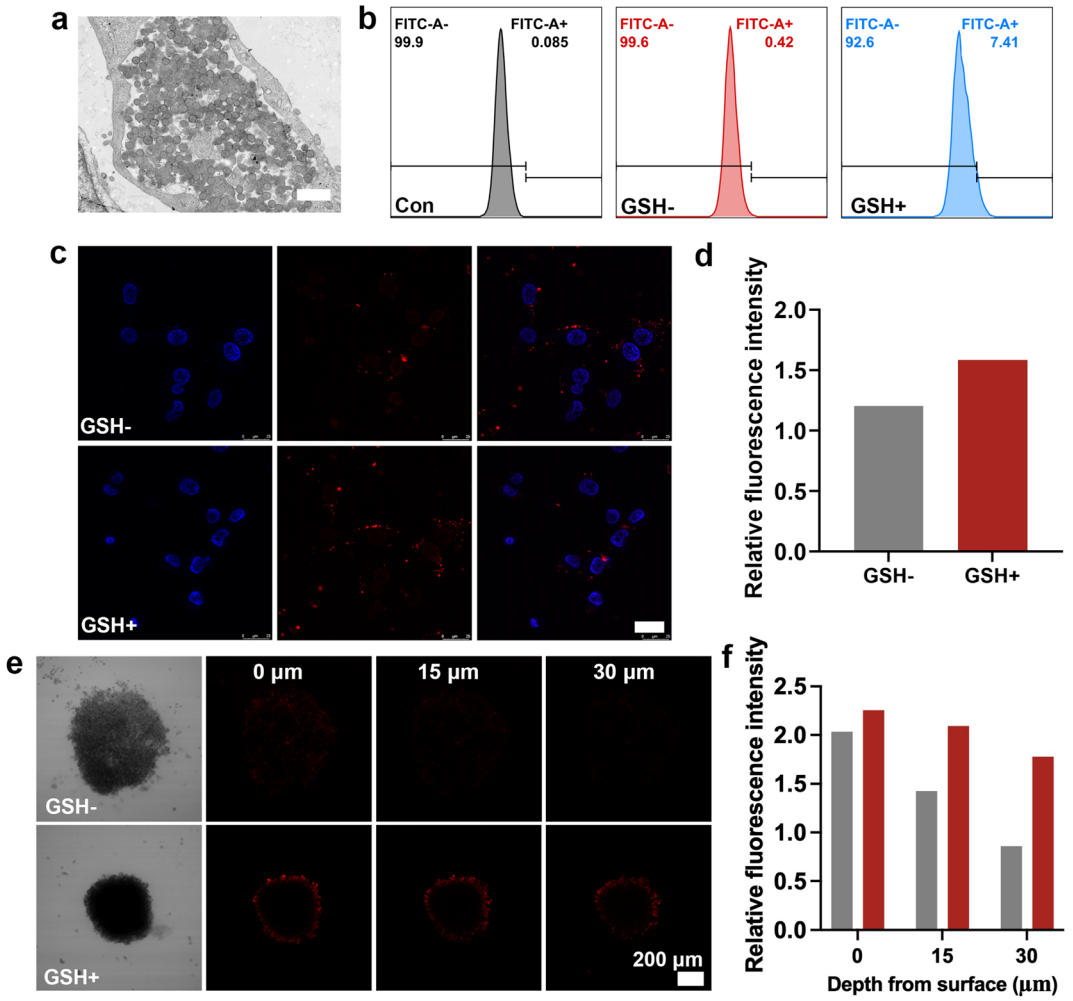

Fig. 3 Bio-TEM images of GSH-treated K7M2 cell after incubation with DMNs (a), flow cytometry (b), CLSM images (c) and quantitative fluorescence intensity (d) of untreated or GSH-treated K7M2 cell after incubation with DMNs, CLSM images (e) and quantitative fluorescence intensity (f) of untreated or GSH-treated multicellular spheroids after incubation with DMNs.

hollow spherical nanoparticles within GSH-treated K7M2 cells, thereby verifying the highly efficient cellular internalization of these DMNs. Furthermore, the morphological distinction of DMNs (existing as intact hollow spheres intracellularly as opposed to collapsed star-shaped nanostructures in ambient air) was ascribed to their robust structural deformability, a property that enabled the DMNs to adopt a compact spherical conformation in aqueous solution. And the flow cytometry results indicated the percentage of GSH treated K7M2 cell in internalized DMNs was 7.41 (Fig. 3b), which was 17.64 times higher than that in untreated K7M2 cell (0.42), demonstrating that instantaneous framework transformation (from stiff Si–R–Mn to soft Si–R–Si) in GSH solution effectively enhanced cellular uptake. Simultaneously, confocal laser scanning microscope (CLSM) images showed that strengthened fluorescence signal of FITC-labeled DMNs appeared in GSH treated K7M2 cell (Fig. 3c) compared to that of without GSH-treated group, demonstrating the enhanced cellular internalization of DMNs in a simulated tumor microenvironment. Quantitative fluorescence intensity results of intracellular FITC-labeled DMNs displayed that the mean fluorescence intensity (MFI) in untreated and GSH treated group were 1.2 and 1.6, respectively (Fig. 3d). The higher MFI in GSH treated K7M2 cell further confirmed more effective cell uptake of DMNs.

Afterwards, the multicellular spheroids penetration of DMNs in simulated TME was further assessed (Fig. 3e). The CLSM images displayed the obvious fluorescence signals in GSH-treated multicellular spheroids at depths from 0 to 30 μm, demonstrating excellent penetration of DMNs. In contrast, the corresponding fluorescence signals was clearly visible at depths of 0 μm within untreated multicellular spheroids, with a notably significant signal reduction observed at 15 and 30 μm. These results suggested that most particles were restricted to the peripheral zone of the multicellular spheroid, with negligible penetration into the inner core. Additionally, the MFI of GSH-treated multicellular spheroids at depths of 0, 15, and 30 μm were 2.3, 2.1 and 1.8 (Fig. 3f), respectively, which were 1.15, 1.5, and 2.25 times higher than those of the untreated group (2.0, 1.4 and 0.8). The significant improvement in multicellular spheroids penetration at 15 and 30 μm was attributed to the

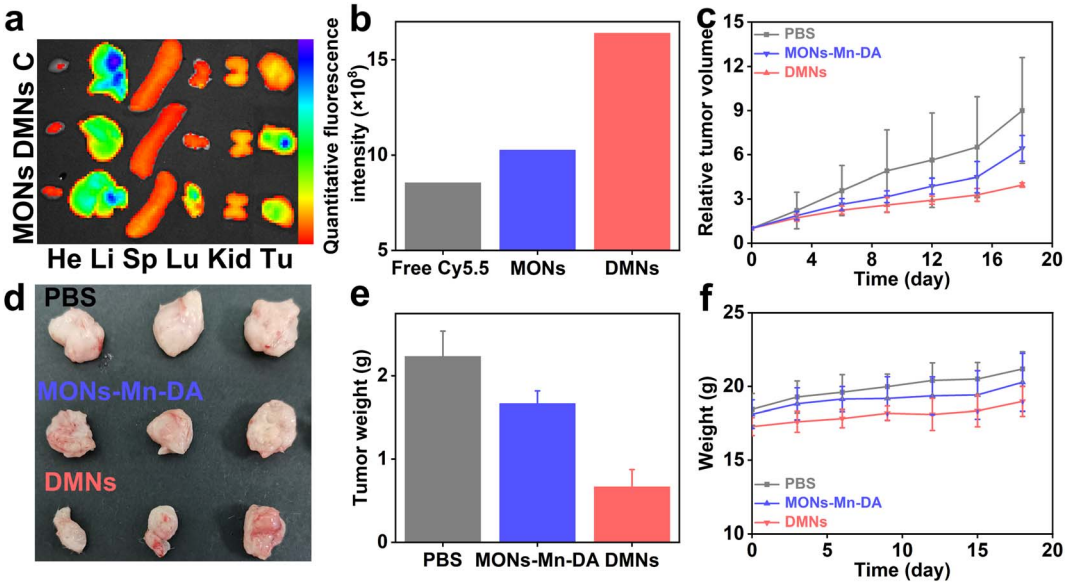

Fig. 4 Excised tissues (heart, liver, spleen, lung, kidney, and tumor) of K7M2 tumor-bearing mice after intravenously injection (a), and quantitative mean fluorescence intensity of tumor (b). Average tumor volume curves (c), optical photos (d), average tumor weights (e) and body weights change curve (f).

superior deformability of soft Si–R–Si framework inside GSH-treated DMNs, which facilitated their extrusion through intercellular spaces or transcellular penetration.

2.4. *In vivo* non-specific biodistribution and tumor-specific chemotherapy

Encouraged by the enhanced cellular uptake and penetration, the DMNs-induced tumor-specific chemotherapy efficacy was further investigated. Before that, the *in vivo* biodistribution of DMNs was investigated (Fig. 4a). The fluorescence imaging results demonstrated that distinct fluorescence signals were detected in the livers of free Cy5.5 or stiff MONs treated groups (4.69×10^9 and 4.62×10^9, Fig. S5), indicating their inevitable nonspecific accumulation. However, markedly attenuated fluorescence signals were observed in the livers of DMNs treated group (2.66×10^9), verifying that, compared to free Cy5.5 and stiff Si–R–Si, Si–R–Mn with appropriate stiffness could effectively reduce their non-specific distribution, which was a critical property for reducing nanoparticle-associated organ toxicity. Furthermore, the highlighted tumor fluorescence signal was detected in MONs- and DMNs-treated group than in the free Cy5.5-treated group, indicating that these nanoparticles enhanced tumor-targeting capacity *via* the enhanced permeability and retention (EPR) effect. In addition, quantitative fluorescence intensity results displayed the MFI of tumor in DMNs-treated group was 16.39×10^8 (Fig. 4b), which was 1.6 time stronger than that in stiff MONs treated group (10.26×10^8). Substantially elevated mean fluorescence intensity (MFI) demonstrates that these DMNs could promote their accumulation in tumor tissues *via* stiffness-transforming properties (maintained stiffness during systemic circulation to evade reticuloendothelial system clearance and softened in response to the tumor microenvironment to enhance tumor accumulation). The decreased liver and spleen biodistribution and increased tumor accumulation of DMNs was highly conducive to enhancing drug concentration and preventing hepatotoxicity.

Then, the DMNs-induced intracellular oxidative stress was investigated (Fig. S6). The CLSM images displayed enhanced fluorescence appearing in the DMNs-treated K7M2 cell, suggesting their excellent oxidative stress regulation effect. And the *in vitro* cytotoxicity of DMNs in normal HeLa cells and tumor K7M2 cells were evaluated, respectively. As Fig. S7 shown, the HeLa cell viability remained above 85% at DMNs concentrations ranging from 0–200 μg mL^{-1}, while the survival rate of K7M2 cell was only 51% at a concentration of 200 μg mL^{-1} demonstrating their selective cytotoxicity. Furthermore, the relative tumor volumes, optical photographs and average tumor weights were recorded to evaluate the antitumor efficacy of DMNs. The tumor volumes curves displayed a gradually increasing volume in PBS-treated group (Fig. 4c), indicating no tumor-suppressive effect. Upon MONs-Mn–DA treatment, the growth of tumor volume slowed down, suggesting the limited tumor inhibition effect. Encouragingly, following the treatment with DMNs, the most pronounced inhibition of tumor volume was observed. Upon 18 days post-treatment, the relative tumor volume (final volume/initial volume) was only 3.95, far lower than that of MSNs-(6.42) or PBS-(8.99) treated group, confirming the effectiveness of DMNs tumor specifical chemotherapy. Meanwhile, the optical photographs (Fig. 4d) and the average tumor weight revealed the minimum volume and mass of tumor (0.63 g) in DMNs treated group than MONs (1.61 g) and PBS (2.28 g) treated group (Fig. 4e). The excellent antitumor efficacy of DMNs was attributed to their enhanced cellular uptake, penetration, and tumor accumulation and Mn–DA induced amplified oxidative stress. In addition, the body weights of

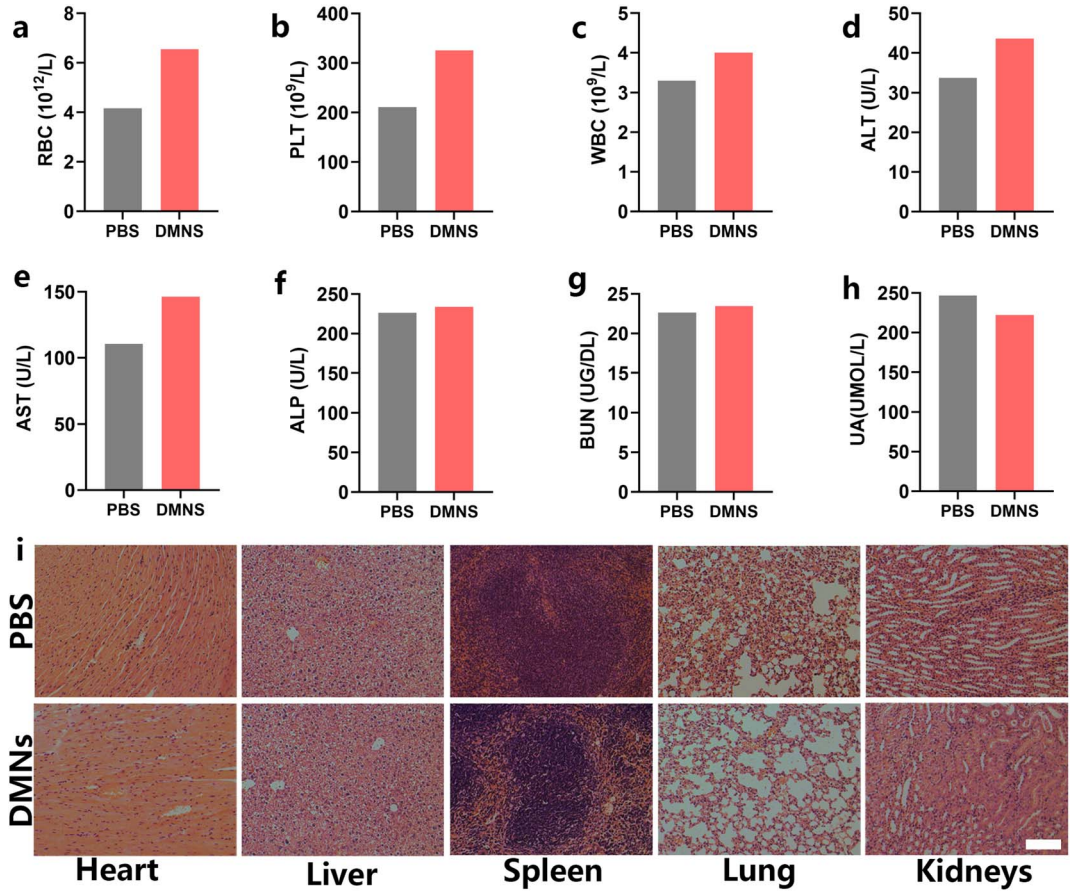

Fig. 5 Quantitative statistical results of serum red blood cell (RBC), platelet (PLT), white blood cell (WBC), alanine aminotransferase (ALT), aspartate aminotransferase (AST), alkaline phosphatase (ALP), blood urea nitrogen (BUN) and uric acid (UA) in PBS, free CDM or CDM NPs treated mice (a–h). H&E staining images (heart, liver, spleen, lung and kidneys) in PBS and DMNs treated mice (i). Scale bar: 100 μm.

these mice presented insignificant fluctuations during the evaluation period, suggesting no systemic side effect (Fig. 4f).

2.5. Biosafety

To further assess their acute and chronic toxicity, biochemical, hematological and histological assay were performed on healthy BALB/c mice injected with DMNs. Biochemical and hematological indicators red blood cell (RBC), platelet (PLT), white blood cell (WBC), alanine aminotransferase (ALT), aspartate aminotransferase (AST), alkaline phosphatase (ALP), blood urea nitrogen (BUN) and uric acid (UA) remained within the normal range (Fig. 5a–h), and H&E staining of major organs (heart, liver, spleen, lung, and kidneys) presented no prominent necrosis, injury, or inflammatory infiltrates (Fig. 5i), suggesting no potential toxicity and highly safe of DMNs for *in vivo* anti-tumor applications. Furthermore, the blood compatibility result displayed that the hemolysis percentage was less than 5% within DMNs concentrations ranging from 0∼200 μg mL^{-1} (Fig. S8), suggesting their excellent hemocompatibility.

3. Conclusion

In summary, PDA coated deformable manganese silicate nanoparticles (DMNs) were successfully synthesized for efficient drug delivery and *in situ* tumor-specific chemotherapy. These DMNs with stiff Si–R–Mn framework, in response to endogenous stimulus (H^+ and/or GSH in the TME), transformed into deformable nanoparticles with soft Si–R–Si framework, accompanied by increased cellular uptake, multicellular spheroids penetration, and tumor accumulation. Meanwhile, the released Mn^{2+} and the DA generated from the depolymerization of PDA are able to *in situ* form Mn–DA complexes. This complex significantly promotes electron delocalization, thereby effectively amplifying cellular oxidative stress and inducing cellular oxidative damage. Taken together, the endogenous TME-responsive DMNs improve the efficiency of drug delivery and minimize drug-related toxicities and side effects through mechanical property transformation and *in situ* drug assembly, offering a highly promising and specific chemotherapeutic strategy for osteosarcoma treatment.

4. Materials and methods

4.1. Materials

Anhydrous ethanol, concentrated hydrochloric acid (HCl, 36–38 wt%), concentrated ammonia aqueous solution ($NH_3 \cdot H_2O$, 25wt%), and sodium hydroxide (NaOH) were purchased from Nanjing Chemical Reagent Co., Ltd (Nanjing, China). Oleic acid

(OA) and potassium permanganate ($KMnO_4$) were bought from Sinopharm Chemical Reagent Co., Ltd (Shanghai, China). Bis [(3-triethoxysilyl)] propyl tetrasulfide (TETS), tetraethyl orthosilicate (TEOS), cetyltrimethylammonium bromide (CTAB), ethylene imine polymer (PEI, Mw ≈ 10 000), dopamine hydrochloride (DA), and glutathione (GSH) were obtained from Sigma-Aldrich Co., Ltd (Shanghai, China).

4.2. Synthesis of deformable manganese silicate nanoparticles (DMNs)

DMNs were synthesized using pre-synthesized mesoporous organosilica as hard template. Typically, 0.16 g [1–21] of CTAB and 1 mL of $NH_3 \cdot H_2O$ were dissolved in 75 mL of water and 30 mL of ethanol at 35 °C. Under vigorously stirring for 1 h, 0.25 mL of TEOS and 0.1 mL of TETS was added to the aforementioned mixture solution simultaneously, with constant stirring maintained for 24 hours. Then the milky white mesoporous organosilica nanoparticles (MONs) were centrifuged (10 000 rpm, 10 min) and washed with ethanol/H_2O. And the residual CTAB inside mesoporous pores of MONs were extracted in 200 mL of ethanol and 40 μL of hydrochloric acid at 60 °C for 12 h. For synthesis of manganese silicate nanoparticles (DMNs), MONs (5.8 mg) was dispersed in PEI solution (5 mL, 10 mg mL^{-1}), with shaking for 4 h. The products were centrifuged and washed for three times. Then these obtained MONs-PEI and $KMnO_4$ (10 mg) were dispersed in 5 mL of water and stirred mildly at 35 °C for 24 h. Afterwards, the brown products were collected by centrifugation and re-dispersed in 5 mL of water and 100 μL of OA stirring for 24 h. The manganese silicate nanoparticles (DMNs) were collected, washed, and re-dispersed in 10 mL of water for further use.

4.3. Stiffness transformation of manganese silicate nanoparticles

DMNs (10 mL) was dispersed in 20 mM of GSH solution (10 mL) stirring for 10 min. The precipitate was redispersed in ethanol for observation under TEM and element mapping.

4.4. Synthesis of polydopamine (PDA) coated manganese silicate nanoparticles

For synthesis of polydopamine (PDA) coated manganese silicate nanoparticles, the resulting MSNs and dopamine hydrochloride (10 mg) were dispersed in Tris buffer (10 mL, pH 8.5, 10×10^{-3} M) stirring for 6 h in darkness. The final products were centrifuged and lyophilized for 48 h.

4.5. Characterizations

The morphology and element distribution of MSNs and DMNs were measured by transmission electron microscopy (HT7700 microscope, Tokyo, Japan), scanning electron microscopy (S4800 microscope, Tokyo, Japan) and FEI Talos F200X electron microscope, respectively.

4.6. Cell culture

The OS cell line (K7M2 cells) was cultured in Dulbecco's modified eagle medium (DMEM) supplemented with 10% fetal bovine serum (FBS) and 1% penicillin/streptomycin at 37 °C with 5% CO_2.

4.7. Cellular uptake

To investigate the internalization of DMNs by K7M2 cells and macrophages, the K7M2 cells were seeded in 6-well plates (1×10^6 cells per well) for 24 h, followed by incubation with DMNs solution or DMNs/GSH solution for 1 and 3 h, respectively. Subsequently, the K7M2 cells were washed with PBS for three times, trypsinized, and re-suspended in 0.5 mL of PBS. The percentages of K7M2 cells associated with DMNs were measured *via* flow cytometer and observed *via* confocal laser scanning microscopy (CLSM). For the preparation of CLSM sample, the K7M2 cells were co-incubated with DMNs solution or DMNs/GSH solution for 1 h. Then the cells were washed with PBS, fixed with paraformaldehyde, stained with DAPI, and observed.

4.8. Multicellular spheroids penetration

Warm agarose medium solution (100 μL, 16 mg mL^{-1}) was injected into 96-well plates and cooled at room temperature for agarose gel formation. Afterwards, 100 μL of K7M2 cells at a density of 1×10^5 cells per well was seeded on the agarose gel and cultured for 2 days for K7M2 multicellular spheroids preparation. The pre-fabricated multicellular spheroids were treated with 10 mM of GSH/medium solution (GSH+) or medium (GSH−) for 0.5 h and then co-incubated with DMNs for another 1 h. Finally, these K7M2 multicellular spheroids were observed *via* CLSM to evaluate the penetration of DMNs.

4.9. *In vitro* ROS generation experiments

The K7M2 cells were seeded into 6-well plates at a density of 1×10^6 cells per well for 24 h. These cells were treated with fresh culture medium, MSNs culture medium solution or DMNs culture medium solution. After another 24 h, the culture media were discarded and these K7M2 cells were stained with DCFH-DA for 30 min. Afterwards, these cells were washed three times for observation *via* confocal laser scanning microscope (CLSM).

4.10. *In vitro* toxicity assays

K7M2 cells were cultured in 96-well plates at a density of 1×10^4 cells per well for 12 h. Then these cells were co-incubated with DMNs at different concentrations for 24 h. Afterwards, the medium was replaced with CCK-8 medium solution (100 μL, $V_{medium}/V_{CCK\text{-}8} = 9$), followed by incubation for another 4 h. The absorbance of solution at 490 nm was measured to investigate cell viability: cell viability = absorbance of DMNs treated group/absorbance of without DMNs treated group × 100%.

4.11. Animals

All animal procedures were performed in accordance with the Guidelines for Care and Use of Laboratory Animals of the Zhongnan Hospital of Wuhan University, and were approved by the Animal Ethics Committee of the Zhongnan Hospital of Wuhan University.

4.12. *In vivo* safety

To determine the *in vivo* safety of DMNs, healthy BALB/c mice were randomly divided into 2 groups ($n = 3$ each group) and injected with PBS or DMNs/PBS solution (250 μg kg^{-1}). After 7 days or 28 days post-administration, the blood routine and biochemical indicators to assess their acute toxicity, and the main organs (heart, liver, spleen, lungs and kidneys) were collected, sectioned, stained with hematoxylin and eosin, and observed to investigate their chronic toxicity.

4.13. *In vivo* biodistribution

The *in vivo* non-specific biodistribution of DMNs was investigated *via* K7M2 tumor xenograft models. Briefly, K7M2 tumor-bearing mice were randomly divided into three groups and intravenously injected with PBS, MONs/PBS, DMNs/PBS suspensions. After 4 h post administration, the main organs (heart, liver, spleen, lung, and kidney) and tumors were collected for fluorescence imaging.

4.14. *In vivo* tumor-specific chemotherapy efficacy

To evaluate their specific chemotherapy effect, K7M2 cells (2×10^6 cells) were subcutaneously inoculated on the BALB/c mice. After the tumors grew to a size of 20 mm^3, the mice were randomly divided into three groups (PBS-treated group, MONs-Mn–Da-treated group, DMNs-treated group). Afterwards, 150 μL of PBS, MSNs/PBS, or DMNs/PBS were intravenously injected after 1-, 3-, and 9- days post administration. The tumor volume ($V = ab^2/2$, a and b represent length and width of the tumor) and body weight were recorded every 1 day to monitor the tumor-specific chemotherapy effect. And the tumors in these mice were collected and weighed after treatment.

Conflicts of interest

The authors declare no conflict of interest.

Data availability

The data supporting this article have been included as part of the supplementary information (SI). Supplementary information: EDS, hydrodynamic size, TEM image, zeta potential, quantitative mean fluorescence intensity, CLSM images, HeLa and K7M2 cell viability and hemolysis percentage. See DOI: https://doi.org/10.1039/d6ra00177g.

Acknowledgements

This work was supported by grants from the International Science and Technology Cooperation Project of Hubei Province (No. 2024EHA063), National Natural Science Foundation of China (22305128) and the Macao Young Scholars Program (AM2025025, Jun Tao).

References

1 M. Harris and C. Hawkins, Recent and ongoing research into metastatic osteosarcoma treatments, *Int. J. Mol. Sci.*, 2022, **23**, 3817.
2 P. Meltzer and L. Helman, New horizons in the treatment of osteosarcoma, *N. Engl. J. Med.*, 2021, **385**, 2066–2076.
3 C. Chen, L. Xie, T. Ren, Y. Huang, J. Xu and W. Guo, Immunotherapy for osteosarcoma: Fundamental mechanism, rationale, and recent breakthroughs, *Cancer letters*, 2021, **500**, 1–10.
4 C. Holohan, S. Schaeybroeck, D. Longley and P. Johnston, Cancer drug resistance: an evolving paradigm, *Nat. Rev. Cancer*, 2013, **13**, 714–726.
5 Z. Jiang, J. Liu, X. Wang, Y. Ma and D. Fu, Current status and prospects of clinical treatment of osteosarcoma, *Technol. Cancer Res. Treat.*, 2022, 21.
6 B. Yang, Y. Chen and J. Shi, Tumor-specific chemotherapy by nanomedicine-enabled differential stress sensitization, *Angew. Chem.*, 2020, **132**, 9780–9788.
7 L. Zhao, X. Wang, M. Jiang, X. Wu, M. Zhang, X. Guan, J. Ma and W. Zhang, A nanosystem of copper (II)-disulfiram for cancer treatment with high efficacy and few side effects, *Front. Mater. Sci.*, 2021, **15**, 553–566.
8 M. Chen, Z. Huang, M. Xia, Y. Ding, T. Shan, Z. Guan, X. Dai, X. Xu, Y. Huang and M. Huang, Glutathione-responsive copper-disulfiram nanoparticles for enhanced tumor chemotherapy, *J. Controlled Release*, 2022, **341**, 351–363.
9 H. Chen, X. Li, M. Huo, L. Wang, Y. Chen, W. Chen and B. Wang, Tumor-responsive copper-activated disulfiram for synergetic nanocatalytic tumor therapy, *Nano Res.*, 2021, **14**, 205–211.
10 W. Wu, L. Yu, Y. Pu, H. Yao, Y. Chen and J. Shi, Copper-enriched prussian blue nanomedicine for *in situ* disulfiram toxification and photothermal antitumor amplification, *Adv. Mater.*, 2020, **32**, 2000542.
11 J. Zhang, Z. Li, Z. Xie, S. You, Y. Chen, Y. Zhang, J. Zhang, N. Zhao, X. Deng and S. Sun, Building of CuO_2@ Cu-TA@ DSF/DHA Nanoparticle Targets MAPK Pathway to Achieve Synergetic Chemotherapy and Chemodynamic for Pancreatic Cancer Cells, *Pharmaceutics*, 2024, **16**, 1614.
12 Y. Chen, X. H. Zhang, D. B. Cheng, Y. Zhang, Y. Liu, L. Ji, R. Guo, H. Chen, X. K. Ren, Z. Chen, Z. Y. Qiao and H. Wang, Near-Infrared Laser-Triggered *In Situ* Dimorphic Transformation of BF2-Azadipyrromethene Nanoaggregates for Enhanced Solid Tumor Penetration, *ACS Nano*, 2020, **14**, 3640–3650.
13 M. Sun, T. Yue, C. Wang, Z. Fan, E. Gazit and J. Du, Ultrasound-Responsive Peptide Nanogels to Balance

Conflicting Requirements for Deep Tumor Penetration and Prolonged Blood Circulation, *ACS Nano*, 2022, **16**, 9183–9194.

14 X. Lin, R. Zhu, Z. Hong, X. Zhang, S. Chen, J. Song and H. Yang, GSH-Responsive Radiosensitizers with Deep Penetration Ability for Multimodal Imaging-Guided Synergistic Radio-Chemodynamic Cancer Therapy, *Adv. Funct. Mater.*, 2021, **31**, 2101278.

15 M. Azizi, R. Esfahlan, H. Samadian, M. Hamidi, K. Seidi, A. Dolatshahi-Pirouz, A. Yazdi, A. Shavandi, S. Laurent, M. Hagh, N. Kasaiyan, H. Santos and M. Shahbazi, Multifunctional nanostructures: Intelligent design to overcome biological barriers, *Mater. Today Bio*, 2023, **20**, 100672.

16 H. Jia, Y. Zhu, X. Liu, G. Pan, G. Gao, W. Sun, X. Zhang, Y. Jiang and F. Wu, Construction of dually responsive nanotransformers with nanosphere nanofiber nanosphere transition for overcoming the size paradox of anticancer nanodrugs, *ACS Nano*, 2019, **13**, 11781–11792.

17 Q. Yang, G. Wu, Y. Yang, Y. Zhou, J. Song, H. Gao and W. Huang, GSH-Responsive Shape-transformable nanotheranostics for dual-modal T1/T2 MRI-guided enhanced PDT of nasopharyngeal carcinoma, *Adv. Funct. Mater.*, 2024, **34**, 2402194.

18 H. Yu, Y. Yu, R. Lin, M. Liu, Q. Zhou, M. Liu, L. Chen, W. Wang, A. Elzatahry, D. Zhao and X. Li, Camouflaged virus-like-nanocarrier with a transformable rough surface for boosting drug delivery, *Angew. Chem., Int. Ed.*, 2023, **62**, e202216188.

19 C. Sun, Y. Liu, J. Du, Z. Cao, C. Xu and J. Wang, Facile Generation of Tumor-pH-labile linkage-bridged block copolymers for chemotherapeutic delivery, *Angew. Chem., Int. Ed.*, 2015, **55**, 1010–1014.

20 J. Tao, Y. Tian, D. Chen, W. Lu, K. Chen, C. Xu, L. Bao, B. Xue, T. Wang, Z. Teng and L. Wang, Stiffness-transformable nanoplatforms responsive to the tumor microenvironment for enhanced tumor therapeutic efficacy, *Angew. Chem., Int. Ed.*, 2023, **62**, e202216361.

21 Z. Teng, C. Wang, Y. Tang, W. Li, L. Bao, X. Zhang, X. Su, F. Zhang, J. Zhang and S. Wang, Deformable hollow periodic mesoporous organosilica nanocapsules for significantly improved cellular uptake, *J. Am. Chem. Soc.*, 2018, **140**, 1385–1393.